Controlling Film Formation and Host-Guest Interactions to Enhance the Thermoelectric Properties of Nickel-Nitrogen-Based 2D Conjugated Coordination Polymers

Hio-Ieng Un, Yang Lu, Jiaxuan Li, Renhao Dong, Xinliang Feng, and Henning Sirringhaus*

2D conjugated coordination polymers (cCPs) based on square-planar transition metal-complexes (such as MO_4, $M(NH)_4$, and MS_4, M = metal) are an emerging class of (semi)conducting materials that are of great interest for applications in supercapacitors, catalysis, and thermoelectrics. Finding synthetic approaches to high-performance nickel-nitrogen (Ni-N) based cCP films is a long-standing challenge. Here, a general, dynamically controlled on-surface synthesis that produces highly conductive Ni-N-based cCP films is developed and the thermoelectric properties as a function of the molecular structure and their dependence on interactions with ambient atmosphere are studied. Among the four studied cCPs with different ligand sizes hexaminobenzene- and hexaaminotriphenylene-based films exhibit record electrical conductivity (100–200 S cm^{-1}) in this Ni-N based cCP family, which is one order of magnitude higher than previous reports, and the highest thermoelectric power factors up to 10 μW m^{-1} K^{-2} among reported 2D cCPs. The transport physics of these films is studied and it is shown that depending on the host-guest interaction with oxygen/water the majority carrier type and the value of the Seebeck coefficient can be largely regulated. The high conductivity is likely reflecting good interconnectivity between (small) ordered domains and grain boundaries supporting disordered metallic transport.

1. Introduction

After their discovery in 1977 and the subsequent nearly half-a-century development, organic (semi)conducting polymers have integrated into our daily life and brought revolutionary changes to semiconductor science and technology and modern display and electronics industry. Exploration of new materials continues to be an engine of progress in performance. One fundamental limitation of linear conjugated polymers is that charge transport is limited by the 1D conjugation along the polymer backbone. 2D conjugated coordination polymers (cCPs) potentially provide a route to much faster charge transport due to the defect-tolerant 2D lattice. According to the definition by International Union of Pure and Applied Chemistry,[1] 2D cCPs are characterized by their repeating coordination units extending in two dimensions, and 2D conjugated metal-organic frameworks (cMOFs) are a subset of 2D cCPs with organic

H.-I. Un, J. Li, H. Sirringhaus
Optoelectronics Group
Cavendish Laboratory
University of Cambridge
JJ Thomson Avenue, Cambridge CB3 0HE, UK
E-mail: hs220@cam.ac.uk

Y. Lu, R. Dong, X. Feng
Center for Advancing Electronics Dresden & Faculty of Chemistry and Food Chemistry
Technical University of Dresden
Mommsenstrasse 4, 01062 Dresden, Germany

Y. Lu, X. Feng
Max Planck Institute of Microstructure Physics
06120 Halle (Saale), Germany

Y. Lu
University of Strasbourg
CNRS
ISIS, UMR 7006
8 Alleé Gaspard Monge, Strasbourg 67000, France

R. Dong
Key Laboratory of Colloid and Interface Chemistry of the Ministry of Education
School of Chemistry and Chemical Engineering
Shandong University
Jinan 250100, China

**ADVANCED
SCIENCE NEWS**

www.advancedsciencenews.com

**ADVANCED
MATERIALS**

www.advmat.de

ligands in the coordination framework containing voids. These synthetic layered materials have been widely demonstrated to be very promising for electrochemical and catalytic applications.[2-8] They have also been theoretically predicted to be promising, synthetically tunable materials for thermoelectrics,[9-11] which has been confirmed by recent experimental studies.[12-14]

Thermoelectric performance is determined by a dimensionless figure of merit $ZT = \sigma S^2 T/\kappa$. To achieve efficient thermoelectric conversion, high electrical conductivity σ and Seebeck coefficient S, and simultaneously low thermal conductivity κ are necessary. These thermoelectric coefficients of 2D cCPs strongly depend on the electronic coupling within the square planar coordination fragment (i.e., MX_4, M = metal and X = O, NH, and S) and the coupling between the coordination fragment and the organic conjugated spacer.[9,11] Good frontier molecular orbital alignment and strong orbital interaction favour enhanced orbital hybridization and wavefunction delocalization, which enable large bandwidth, small effective mass, and long relaxation time that enhance carrier mobility and thus thermoelectric properties.[9,11] –OH, –NH$_2$, and –SH are the most widely used functional groups in constructing 2D cCPs. O-coordinated 2D cCPs usually have relatively localized wavefunction and narrow bandwidth and exhibit relatively poor charge transport properties (electrical conductivities are usually only $10^{-8} – 0.1$ S cm^{-1} for pellets and $10^{-4} – 1$ S cm^{-1} for films and crystals),[15-21] while S-coordinated ones tend to show delocalized wavefunction and wide bandwidth, and thus high conductivities of up to 1 000–2 500 S cm^{-1} in films.[22-25] However, their Seebeck coefficients are very small ($|S| < 10$ μV K^{-1}), typical for metals.[22-25] N-coordinated 2D systems seem to lie in between, showing moderate electrical conductivity of $10^{-4} – 58.8$ S cm^{-1} for pellets and $10^{-3} – 40$ S cm^{-1} for films so far and, importantly, relatively larger Seebeck coefficient ($|S| = 10 – 400$ μV K^{-1}).[12,13,26-32] They could hence potentially be more promising for thermoelectrics than their more conducting S-coordinated cousins.

The electrical conductivity of Ni-N-based 2D cCP films can be substantially enhanced through more advanced methods of film synthesis.[29–35] One challenge for the synthesis of this family is the limited ambient stability and solubility of multi-NH$_2$ aromatic compounds. Typically, free multi-NH$_2$ aromatic compounds are very reactive against oxidizing agents such as oxygen. To prevent irreversible oxidation of such starting materials, N-based ligands are typically available as hydrochlorides. As their hydrochlorides are highly soluble in water and hardly soluble in orthogonal organic solvents, the efficient liquid-liquid interfacial synthesis which has been widely used for S-coordinated cCPs is not compatible.[22,25,36] In addition, the stronger coordination bond of Ni-N than that of Ni-S tends to lead to more irreversible bond formation, resulting in poorly crystalline or amorphous products.[37] N-based 2D cCPs are therefore mostly synthesized with hydrothermal methods in open systems, but this method provide powders and thus only pellet samples are typically available.[12,26,28]

Even though some of the N-based cCPs are computationally predicted to have delocalized wavefunction and promising thermoelectric properties,[5,9–11,26,38].the conductivities of films achievable so far remain relatively low (< 40 S cm^{-1}) and usually exhibit strong thermally activated behavior as a function of temperature[26,32,34]; experimental evidence confirming efficient charge delocalization is often lacking. Due to the lack of a general method for controlled film fabrication, controlled studies of structure-property relationship have been hampered so far.
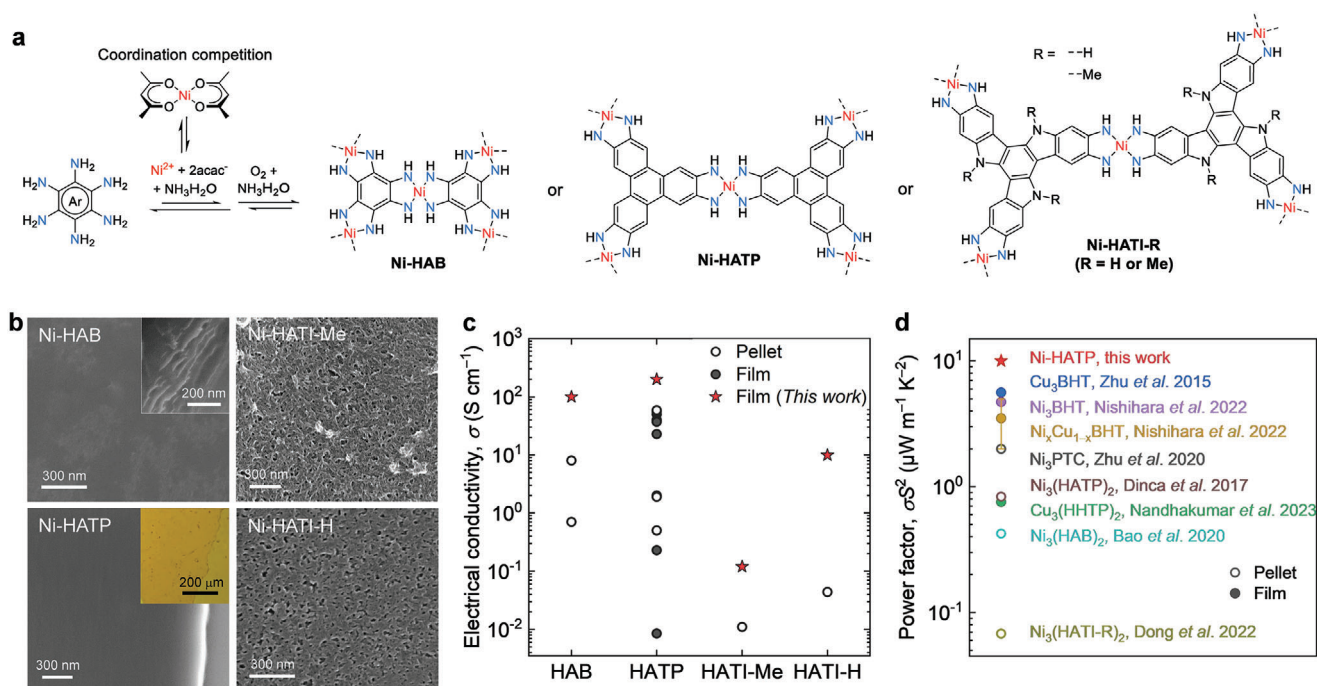
Herein, we report record electrical conductivity (100–200 S cm^{-1}) with (near) metallic transport characteristics in thin films for this Ni-N-coordinated 2D cCPs and the highest power factors (10 μW m^{-1} K^{-2}) reported to date for 2D cCPs. High-performing thin films were synthesized by a dynamically controlled method through introducing coordination competition developed in this work. The universality of this method is demonstrated with four materials with different linker sizes and different carrier types (holes and electrons). We further investigate the dependence of their thin-film thermoelectric properties on host-guest interaction with ambient adsorbates (O$_2$ and H$_2$O) residing in the framework and find that such host-guest interaction can substantially modulate/enhance thermoelectric performance and power factors by 60 times. We apply a heterogeneous transport model to explain some of the salient features of the charge transport physics of these systems.

2. Synthesis and Characterizations

To explore and develop the synthesis method for highly conductive Ni-N-based cCP films, we used the hexaminobenzene (HAB) linker as a model system. We investigated and optimized the use of different precursors of Ni(II) ion, bases, their stoichiometries, as well as solvents, in terms of their influences on the form of the final product (thin films on the surface versus powders in the solution). A full list of the reaction conditions, which we have screened, can be found in Table S1 (Supporting Information).

Reactions were setup under nitrogen atmosphere by adding a certain amount of freshly dissolved aqueous solutions of base, Ni(II) salt, and organic ligand into a small vial in sequence at 45 °C. The reaction systems were then removed from nitrogen to ambient air, where the non-airtight sealing of the vials allowed slow air diffusion. After being left in air overnight at 45 °C thin films were formed at the air-liquid interface (see Section 1, Supporting Information for details). Previous work reported that the use of weak base such as NaOAc instead of strong base (NH$_4$OH) is helpful to significantly improve the crystallinity and thereby electrical conduction of powders of N-based cCPs through slowing down nucleation and growth rates and improving reversibility.[28] However, we found that using NaOAc either only yields powders (Figure S1, Supporting Information) or simultaneously generates inhomogeneous (rather than desired smooth, homogeneous) films on the surface with a moderate conductivity of 0.34−5.0 S cm^{-1} (Figures S3−S5, Supporting Information). We designed a competing coordination reaction to slow down the reaction kinetics (**Figure 1a**) and we found that the key synthetic steps to achieve high conductivities in thin films are:

i. Using Ni(acac)$_2$ as the metal ion source to slow down the reaction through introducing coordination competition;

ii. Setting the reaction up under an N$_2$ atmosphere and transferring the non-airtight-sealed system to air after-

2312325 (2 of 11)

**ADVANCED
SCIENCE NEWS**

www.advancedsciencenews.com

**ADVANCED
MATERIALS**

www.advmat.de

Figure 1. Synthesis, film microstructure and summary of thermoelectric performance of Ni-N-based 2D cCP films. a) Designed coordination-competing reaction and the chemical structure of the cCPs synthesized in this work. b) SEM and optical images of the cCPs films. The inset of Ni-HATP is an optical image taken under yellow light. c) Comparison of electrical conductivities of Ni-N-based cCPs with different ligands achieved in this work with corresponding pellets and films reported in the literature. d) Comparison of power factors of our Ni-HATP films with those of other 2D cCPs reported in the literature.
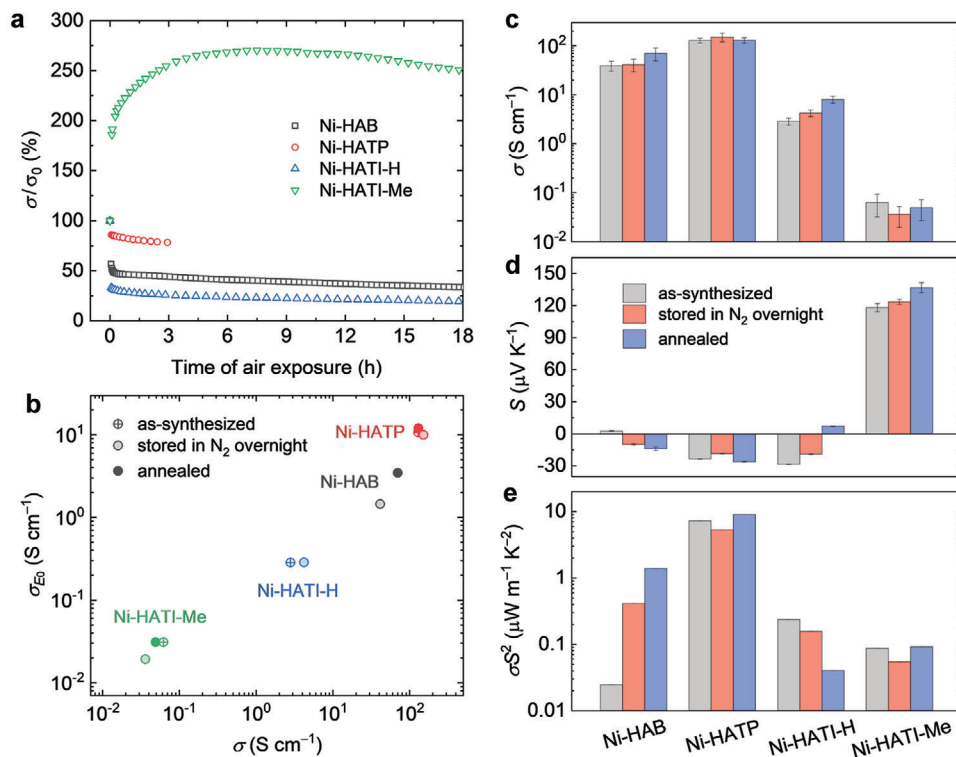
ward to allow slow air diffusion and to prevent rapid (deprotonation-)oxidation of the linker;

iii. Using NH_4OH as base, rather than NaOAc which possibly introduces negative charges on the nanosheet with Na ion as the counter ion intercalated.[34]

The oxidation is one of the key steps in the process (see Section 1 and Scheme S1, Supporting Information for details). When the reaction was setup with an identical recipe but kept in the glovebox, the solution remained clear without any product forming even after 19 h whereas mixtures, that were set up in the glovebox with airtight sealing and then transferred to ambient air, became only slightly dark after 15 h. Once the vials were opened in air, they turned dark rapidly, and powders formed in less than 2 h without films on the surface (Figure S8, Supporting Information). The level of sealing against air ingress, i.e., the diffusion rate of air into the solution, has a strong influence on the reaction dynamics, the form of the products (i.e., powders vs films), and their electrical performance (see Figure S9, Supporting Information for details of the sealing).

Our optimized recipe allowed achieving a four-point-probe (4pp) conductivity of 93 S cm^{-1} in Ni-HAB films after annealing in N_2. This is the highest conductivity reported to date for Ni-HAB. It is worth noting that the electrical conductivities reported here may be underestimated, since there are quite some powder-contaminants underneath the films as well as occasional micro-cracks (Figures S10–S12, Supporting Information).

The surface morphology of the produced Ni-HAB film is smooth and a clear sheet structure can be found at the edge of the film (Figure 1b). Energy-dispersive X-ray spectroscopy (EDX) characterization (Figure S13a, Supporting Information) reveals the presence of the necessary elements C, N, and Ni, but unexpected O is also present. Combined with the results of elemental analysis in which lower percentage of Ni/linker and higher percentage of C/N than expected is found, we reasonably speculate that, some acac anions are trapped within the films, in the forms of either Ni(acac)$_2$ and/or interacting with the central metal ion of the conducting network, as well as byproducts such as hydroxides and oxides. The presence of byproducts was observed in a previous study in which NH_4OH was used.[4] Fourier transform infrared (FTIR) and Raman spectroscopy were employed to probe the chemical moieties present. In FTIR (Figure S13b, Supporting Information) there are clear features in the region of 3 000—3 300 cm^{-1}, 1 300–1 700 cm^{-1}, and ≈1050 cm^{-1} attributed to N–H, C = N and/or C = C (as well as C = O for acac), and C–N vibrations, respectively. In Raman spectra (Figure S13c, Supporting Information) peaks ≈425 cm^{-1}, 600 cm^{-1}, and 1 100–1 700 cm^{-1} attributed to metal-N, C–N, and aromatic ring sp^2 C vibration are found.[4,26] These spectroscopic results show that the films have the expected chemical bonds, suggesting the successful formation of the coordination network. Usually the amino N–H group is expected to show two bands ascribed to antisymmetric and symmetric stretching vibrations, whereas the imino N–H exhibited only one N–H stretching vibration band.[42,43] The absence of a second band at ≈3 390–3 400 cm^{-1} in our spectrum indicates that there is negligible amount of amino group and the imino group coordinates to the Ni center.[42,43] Both the FTIR

**ADVANCED
SCIENCE NEWS** _____

www.advancedsciencenews.com

**ADVANCED
MATERIALS**

www.advmat.de

Figure 2. Influence of ambient adsorbates on conductivity and thermoelectric properties of Ni-N-coordinated 2D cCPs. a) Electrical conductivities as a function of air exposure time. b) Transport coefficient extracted with $s = 1$ from the Kang-Snyder model versus electrical conductivity. The data points of as-synthesized Ni-HAB and annealed Ni-HATI-H are not included since they probably involve two-band transport which cannot be described by the Kang-Snyder model that was built based on a single band. c–e), Electrical conductivities, Seebeck coefficients and power factors of the four cCPs right after synthesis, after storage in N_2 overnight, and after annealing at 125 °C for 90 min respectively. In the as-synthesized films, oxygen and water are adsorbed, while storing in N_2 overnight and annealing are effectively degassing the films.

and Raman spectra are essentially the same as for the previously reported crystalline structure.[44,45] However, all films produced by our method are poorly crystalline (Figure S14, Supporting Information): In X-ray diffraction (XRD) only a broad diffraction peak with very low intensity centred at $2\theta \approx 30°$ is observed. In grazing-incidence wide-angle X-ray scattering (GIWAXS) only a low-intensity arc in the out of plane direction, attributed to face-on $\pi{-}\pi$ stacking are observed, indicating a poor long-range order due to extremely small particle sizes (i.e., Scherrer broadening).[38–41] This can also be envisioned as layered networks that are randomly shifted in-plane with respect to the adjacent layers.[39]

To prove the applicability of this synthesis approach to a wide range of Ni-N-based 2D cCPs, three more linkers with different size – hexaaminotriphenylene (HATP), hexaiminotriindole with and without methylation (HATI-Me and HATI-H) – were also employed (Figure 1a). All thin films present very smooth and homogeneous surface morphology while the two HATI-based cCPs show less compact film structure, with pinholes seen (Figure 1b). The highest conductivities of these synthesized films achieved are 2.0×10^2 S cm^{-1} for Ni-HATP, 10 S cm^{-1} for Ni-HATI-H, and 9.0×10^{-2} S cm^{-1} for Ni-HATI-Me. These results are higher than those previously reported for each of the four cCPs (Figure 1c). In Figure 1d we compare the thermoelectric power factors of our Ni-HATP films to that of other 2D cCPs reported in the literature (for

details see below). We also measured the thermal conductivity of our highest-performing Ni-HATP films to be 0.37 W m^{-1} K^{-1} at room temperature, from which we can estimate a ZT value of 8.1×10^{-3}, which to the best of our knowledge is the highest thermoelectric performance in both p- and n-type 2D cCPs reported to date.

3. Host-Guest Interaction-Modulated Thermoelectrics

We investigated the dependence of the electrical conductivity on exposing the films to air. For Ni-HATI-Me the conductivity rapidly increased about twice in the first 5 min and then slowly decreased after 9 h, while for the other three cCPs electrical conductivities were reduced to 30 – 85% once (< 5 min) exposed to ambient air (**Figure 2a**). We note that in all samples there are two main regimes: an initial response regime lasting for fewer than 10 min for Ni-HAB, Ni-HATP, and Ni-HATI-H and ≈3 h for Ni-HATI-Me, in which the conductivity changes rapidly, and a second regime, in which the conductivity changes more slowly (Figure 2a). We attribute the immediate response to (physical and/or chemical) adsorption of oxygen and/or moisture in air and the slow dynamic to (electro)chemical degradation of the materials.[46–48] In the process of (electro)chemical degradation, oxygen with or without water usually captures electron

ADVANCED
SCIENCE NEWS

www.advancedsciencenews.com

ADVANCED
MATERIALS

www.advmat.de
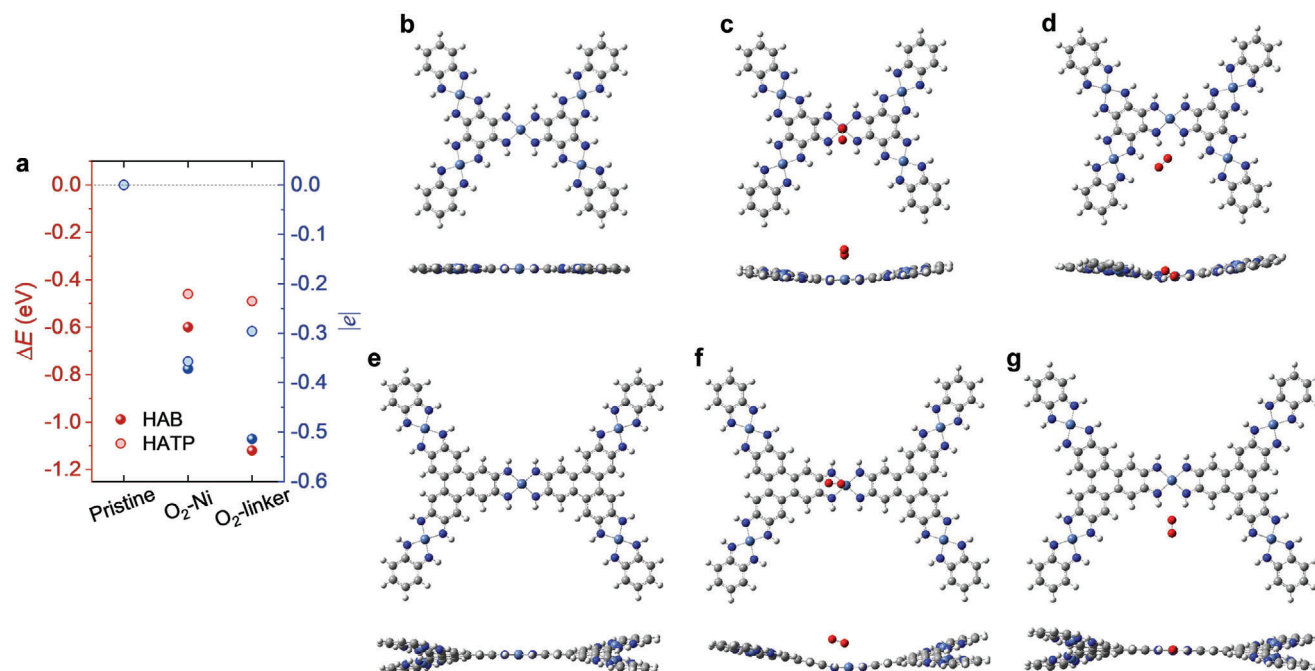
Figure 3. DFT calculations of the adsorption and binding of O_2 in Ni-HAB and Ni-HATP. a) Summary of free energy changes (left axis, red) and charge transfers (right axis, blue) after interacting with O_2 where pristine structure is defined as 0 as reference. b–d) Molecular conformations of pristine Ni-HAB, O_2 interacting with the open metal site of Ni-HAB and O_2 interacting through a hydrogen bond with the organic linker of Ni-HAB, respectively. e–g) Corresponding molecular conformations for pristine Ni-HATP, O_2 interacting with the open metal site of Ni-HATP and O_2 interacting through a hydrogen bond with the organic linker of Ni-HATP. Both side views and top views are shown.

carriers from the materials and forms hydroxide (HO^-) and water may potentially damage the square-planar coordination units through interacting with coordination-unsaturated metal sites. Consistently, electrical measurements under environmental control (Figure 2c) reveal that for as-synthesized Ni-HAB, Ni-HATP, and Ni-HATI-H films, annealing or storing in N_2 atmosphere is helpful to enhance the electrical conductivities by 77%, 18%, and 180%, respectively, probably through degassing of the adsorbed molecules and not through improvement of the microstructure since their morphologies before and after annealing are identical (Figures S15 and S16, Supporting Information). The mechanism for the experimentally observed, degassing-induced enhanced electrical conduction upon annealing or storing in N_2 (Figure S18, Supporting Information) is consistent with the general scientific understanding of gas adsorption in MOFs[48–51] and with the electronic structure model discussed below. Further discussion can be found in Section 3 (Supporting Information). For Ni-HATI-Me, on the other hand, both treatments (annealing or storing in N2) are harmful. These results are consistent with the transport properties observed upon air exposure.

We also measured the Seebeck coefficient under the same environmental control. Only in Ni-HATP and Ni-HATI-Me the Seebeck coefficients exhibit a consistent sign, independent of treatment, negative for Ni-HATP and positive for Ni-HATI-Me. In comparison, after degassing, the Seebeck coefficient of Ni-HAB switches sign from positive with very small value to negative and Ni-HATI-H switches from negative to positive (Figure 2d). A sign change of Seebeck coefficient (i.e., switch of majority carrier

type) due to the environment/interaction with adsorbed species has also been observed in other 2D cMOFs.[27,52] The oriented d-orbitals of the metal can act as electron acceptors, while polar heteroatoms and hydrogen atoms of the ligands provide weak bonding sites with surrounding molecules. These non-covalent, host-guest interactions with adsorbates are likely to be generally present in 2D cCPs.

To better understand the impact of host-guest interaction with O_2 and H_2O on electronic properties, density functional theory (DFT) calculations were performed. Since the thermoelectric response of the cCPs films upon host-guest interaction falls into two groups – either leading to a sign change of the Seebeck coefficient or not, we selected Ni-HAB and Ni-HATP as model compounds for these two groups. We consider bonding mechanisms between oxygen/water molecules and the linking units through formation of hydrogen bonds and with the metal centres through coordination interactions. We find that interactions with O_2 (**Figure 3**) are stronger than with H_2O (Figure S19, Supporting Information), as seen by the more negative free energy changes. Our results can be mainly divided into two categories: Metal-center bonding is associated with negative free energy change ($\Delta E < 0$) and a pronounced structural relaxation (Figure 3c,f; Figure S19c,f, Supporting Information) while bonding with the linker does not lead to as strong structural relaxation (Figure 3g; Figure S19d,g, Supporting Information) except for the Ni-HAB-O_2 complex (Figure 3d). This suggests that the host-guest interaction is more favorable to be linker-centered than open metal site-centered from a kinetic perspective since there is no need to overcome the energy barrier for structural relaxation. The negative

free energy change upon interacting with either H$_2$O or O$_2$ indicates that both the formation of an O$_2$ and H$_2$O complex is thermodynamically favorable in Ni-HAB and Ni-HATP (Figure 3a; Figure S19a and Tables S2,S3, Supporting Information), with a larger free energy change predicted for the O$_2$ complex with the linker. Because this stabilization energy of the structural distortion coupled with charge localization is large, for example, $\Delta E = -1.1$ eV for Ni-HAB-O$_2$ linker complex (Figure 3a,d), such a complex is therefore likely to be stably present, when exposing films to air or O$_2$. The linker is likely to act as the most active site dominating the interaction with O$_2$ while the metal ion modulates the electronic density of the host material. Similar results were also observed in previous theoretical and experimental studies.[53–55]

In Ni-HAB the negative sign of Seebeck coefficient of the annealed films indicates that charge transport is electron-dominant; this is potentially consistent with theoretical band structure calculations that predicted the Fermi level to lie around a steep, dispersive electron pocket and a comparatively flat hole band.[56] Interaction with H$_2$O has very little change in the charge density of Ni-HAB (0–0.085). After the formation of the complex with O$_2$, however, significant charge transfer from Ni-HAB to O$_2$ (i.e., oxidation) is induced, −0.372 for O$_2$-Ni interaction and −0.514 for O$_2$-linker interaction (Figure 3a; Figure S19a and Table S4, Supporting Information), leading to light p-type doping with the Fermi level shifting down in energy toward the hole band. Since the energy against wave vector of the hole-dominant band is predicted to be rather flat resulting in small group velocity and comparatively large effective mass,[56] this simple two-band framework can explain both the sign change (from negative to positive) of the Seebeck coefficient, and the reduced conductivity observed in Ni-HAB after O$_2$ absorption. The small magnitude of the Seebeck coefficient in the as-fabricated Ni-HAB films, which have had some O$_2$ exposure during film processing, is therefore likely to reflect a competition between contributions from the electron and the hole bands. The Seebeck coefficients of hole and electron have opposite signs and therefore tend to cancel each other, under conditions where both bands contribute to the conduction. It is possible that other factors contribute as well, such as changes in the electronic structure owing to the contribution of the orbitals of oxygen or the formation of trap sites or scattering centres associated with the bound O$_2$ molecules in the framework. The less favorable host-guest interaction of O$_2$ with Ni-HATP than with Ni-HAB (in both free energy change and charge transfer aspects, shown in Figure 3a; Table S4, Supporting Information) is potentially consistent with the more robust and stable n-type transport and the higher thermoelectric performance of Ni-HATP than Ni-HAB. Band structure calculations have also been reported for Ni-HATI-H and Ni-HATI-Me,[12,57] and they show that also in these two systems the Fermi level is close to an electron and a hole bands. This makes it likely that the sign change in the Seebeck coefficient of Ni-HATI-H upon annealing from n- to p-type also arises due to a competition between the two bands.

To better understand the transport processes in these cCPs, we analyse our thermoelectric data within the Kang-Snyder model,[58] which is based on the Boltzmann transport formalism and has been found to be a helpful model for interpreting the transport coefficients in organic conducting polymers. In this model the energy dependent conductivity or transport function $\sigma_E(E, T)$ is expressed as:

$$\sigma_E(E,\ T) = \begin{cases} 0, & (E < E_t) \\ \sigma_{E0}(T) \times \left(\frac{E-E_t}{k_B T}\right)^s, & (E \geq E_t) \end{cases} \quad (1)$$

The transport function describes the contribution that electron states with energy E would make to the total conductivity at temperature T, if they were close to Fermi level E_F. E_t is the energy of the transport edge, s is a power-law energy dependence, and k_B is the Boltzmann constant. The temperature-dependent pre-factor of the transport function $\sigma_{E0}(T)$ is called the transport coefficient[58,59]; it is material-specific and captures the relevant (hopping) transport physics, including the effects of energetic disorder, electron-phonon coupling, interactions between carriers, and effective mass.[58,59] The transport coefficient allows comparison between different thermoelectric materials; the larger σ_{E0} the larger the electrical conductivities at a given E_F position (or reduced chemical potential η). η, on the other hand, determines the Seebeck coefficient, therefore a large σ_{E0} tends to favor high thermoelectric power factors. σ_{E0} can be extracted by using the measured electrical conductivity and the reduced chemical potential $\eta = (E_F - E_t)/k_B T$ which can be evaluated from the measured Seebeck coefficient (see Section 5, Supporting Information for details). In this analysis we exclude the data points / conditions in Figure 2d in which the Seebeck coefficient is very small, i.e., the as-synthesized films of Ni-HAB and the annealed films of Ni-HATI-H, because their small Seebeck coefficient most likely arises from a two-band, electron-hole competition (as argued above). We also assume $s = 1$, which has been found for conducting polymers, such as PEDOT. A validation of this assumption would require producing films with a wider range of conductivities. This would require efficient methods of doping, which have not been developed for these 2D cCPs yet. The plot of transport coefficient against electrical conductivity shows a clear materials dependence; while film treatment modulates electrical properties of different cCPs, somewhat, there are large differences in σ_{E0} between the four materials. Ni-HATP exhibits the highest value of σ_{E0} on the order of 10 S cm^{-1} (Figure 2b), while Ni-HATI-H and Ni-HATI-Me exhibit two orders of magnitude smaller σ_{E0}. This is potentially consistent with the band structure calculations in the literature,[12,57] which show that in Ni-HATI-H and Ni-HATI-Me both the electron and the hole bands near E_F have a relative flat dispersion and large effective masses, while in Ni-HAB and Ni-HATP the electron band has a stronger dispersion and smaller effective mass. This is the likely reason for the higher values of σ_{E0}.

4. Transport Mechanism

As the best performing thermoelectric system Ni-HATP was used as a model system to explore the transport physics in more detail. Temperature dependent measurements of the conductivity and the Seebeck coefficient were performed under high vacuum, after annealing the films until the electrical conductivity did not change over time. Typically, charge transport is categorized into two limiting regimes – metallic, delocalized transport and localized, hopping transport. The former, usually observed in wide

**ADVANCED
SCIENCE NEWS**

www.advancedsciencenews.com

**ADVANCED
MATERIALS**

www.advmat.de
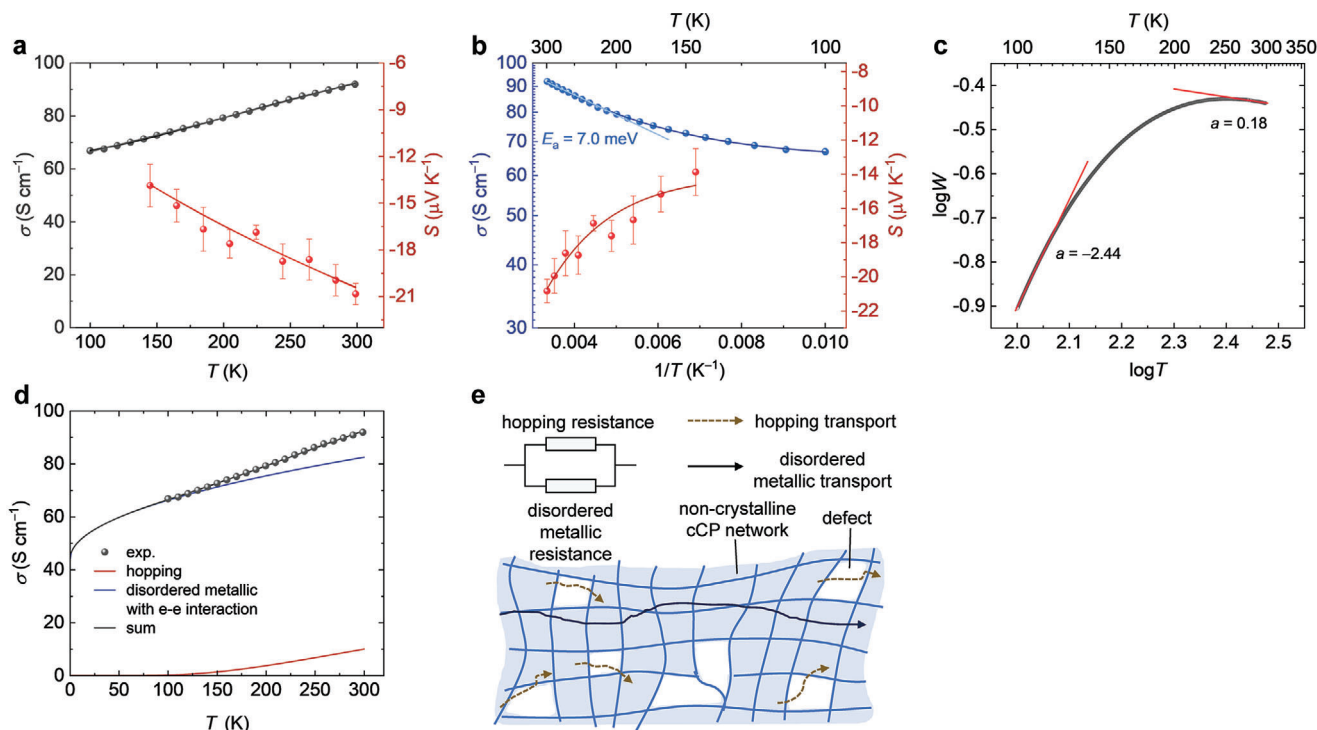
Figure 4. Temperature-dependent thermoelectric transport analysis in layered cCP Ni-HATP. a) Electrical conductivity and Seebeck coefficient as a function of temperature. b) Plot of the electrical conductivity and Seebeck coefficient versus inverse temperature, showing inconsistence with nearest-neighbour hopping, mobility edge, and polaron hopping models. c) Zabrodskii analysis of the measured temperature-dependent conductivity. d) Decomposition of the measured electrical conductivity into contributions from disordered metallic and hopping transport pathways at the grain boundaries. e) Schematic illustration of heterogeneous transport in poorly crystalline 2D cCPs.

band systems with weak electron-phonon coupling and low disorder, is characterized by the conductivity increasing with decreasing temperature, while in the latter, commonly found in narrow bandwidth systems with strong disorder and electron-phonon coupling, the conductivity reduces strongly with decreasing temperature. Models capable of capturing both localized and delocalized transport have also been developed for an intermediate regime between these two limiting cases.[58,59,60] In Ni-HATP we observe a decrease of conductivity with decreasing temperature (**Figure 4**a), which is a clear manifestation of some disorder limiting transport at low temperatures. However, the temperature dependence is relatively weak, between room temperature and 100 K the conductivity only reduces by little more than 30%. The Seebeck coefficient was also found to decrease with decreasing temperature. We attempted to fit the observed temperature dependence of the conductivity and the Seebeck coefficient to widely used models including variable range hopping (VRH), nearest-neighbour hopping (NNH), mobility edge (ME), and polaron hopping (PH). The VRH model describes the electrical conductivity as $\sigma \propto \exp(-T_0/T)^{1/(1+d)}$ and Seebeck coefficient $S \propto T^{(d-1)/(d+1)}$ with d = 3, 2, and 1 for 3D, 2D, and 1D transport. The Efros-Shklovski (E–S) hopping model, which takes into account Coulomb interactions between carriers, predicts $\sigma \propto \exp(-T_0/T)^{1/2}$ and a temperature independent Seebeck coefficient.[61] Our measured S can plausibly be fitted to either $T^{1/2}$ and $T^{1/3}$, but both $\log\sigma - T^{(-1/4)}$ and $\log\sigma - T^{(-1/3)}$ plots apparently deviate from the expected linear dependence (Figure

S23, Supporting Information). Other hopping-dominating transport models NNH, ME, and PH, with $\sigma \propto \exp(-E_a/k_BT)$ and $S \propto E_a/k_BT$, predict $\log\sigma - T^{-1}$ and $S-T^{-1}$ plots are linear and have a same slope[62,63]; however our data largely deviate from both linear mathematical expressions (Figure 4b). Zabrodskii analysis,[64] given by $\log W \approx \log(aT_0^a) - a\log T$ with $W = \frac{d\log\sigma}{d\log T}$, was also employed and we find $a < 0$ over a large temperature range of interest (Figure 4c), which can be interpreted as a signature of presence of metallic states. Combined with the very small activation energy of 7.0 meV at near room temperature, the extrapolated non-zero electrical conductivity at the zero-temperature limit (i.e., $\sigma \neq 0$ as $T \to 0$), and the quite linear temperature dependence of Seebeck coefficient, these experimental observations suggest that electronic conduction in Ni-HATP involves both metallic and localized states. Through introducing an energy dependent term $\sigma_0\exp(-W_H/k_BT)$ (instead of an energy-independent prefactor σ_{E0} in the Kang-Snyder model), the semi-localized transport (SLoT) is in principle capable for capturing both localized, hopping and delocalized, metallic transport in the intermediate regime.[58,59] Starting with an extracted value of 12 for the reduced Fermi level $|E - E_t|/(k_BT)$ according to the measured Seebeck coefficient of ≈ -20 μV K^{-1} at room temperature, we find however our experimental data deviates significantly from what this model predicts (Figure S24, Supporting Information).

The behavior observed in our 2D cCPs is reminiscent of that observed in many conducting polymers and is probably best

**ADVANCED
SCIENCE NEWS**

www.advancedsciencenews.com

**ADVANCED
MATERIALS**

www.advmat.de

understood in terms of a heterogeneous transport model.[65,66] This assumes that metallic conduction is supported in small ordered, crystalline regions that are separated by disordered grain boundaries. The conductivity of such a heterogeneous system can be modeled by considering a network of resistors, with contributions from crystalline domains and grain boundaries taken in series and several pathways that contribute to the conduction through the grain boundaries in parallel. In this model the temperature dependence of electrical conductivity is written as:

$$\sigma(T)^{-1} = (g_m \sigma_{m0})^{-1} \exp\left(-\frac{T_m}{T}\right)$$

$$+ \left[g_h \sigma_{h0} \exp\left(-\frac{T_0}{T}\right)^{\gamma} + \left(g_d \sigma_d + g_d \alpha T^{\frac{1}{2}}\right)\right]^{-1} \quad (2)$$

The first term represents the metallic transport in the crystalline domains, where T_m is a characteristic temperature that reflects the energy of phonons that backscatter carriers. The second term reflects variable-range hopping conduction through the grain boundaries with characteristic hopping temperature T_0 and dimension-dependent exponent γ. The third term reflects disordered metallic transport through the grain boundaries and includes an approximately constant conductivity term and a $T^{\frac{1}{2}}$-dependent term that reflects electron-electron interactions. g_i are geometry factor that considers how much a certain transport pathway contributes to the total conduction, and σ_{i0} are conductivity pre-factors. We find that no matter what value we take for T_m, the metallic term is always near zero from the fit, which means that the transport is strongly grain boundary limited. This suggests that the ordered, crystalline domains are small, which is consistent with the absence of a clear crystalline diffraction signature in XRD. The extracted contributions to the grain boundary-limited conductivity from 2D hopping transport and from disordered metallic transport are shown as a function of temperature in Figure 4d and Figure S25 (Supporting Information). This analysis shows that disordered metallic conduction is the dominant conduction pathway through the grain boundaries at low temperature (100 K), while the hopping transport pathway begins to make contributions to the conductivity toward room temperature. This suggests that the high conductivity observed in Ni-HATP is primarily a result of a good film continuity and good interconnectivity between small, ordered domains. The grain boundaries are not highly disordered, and support relatively efficient disordered metallic transport as opposed to hopping transport (Figure 4e).

5. Conclusion

By developing a dynamically controlled, generally applicable on-surface synthesis approach through introducing coordination competition, we synthesized a range of high-performing 2D cCP films with different carrier types and linker sizes and achieved record electrical conductivity (100–200 S cm^{-1}) in the family of Ni-N-based 2D cCPs and the highest power factor (10 μW m^{-1} K^{-2}) among reported 2D cCPs. Our charge transport analysis is consistent with recent band structure calculations, which show that the Fermi level lies in between an electron

and a hole band in these materials. Depending on film processing and host-guest interactions with atmospheric species, such as O$_2$, small shifts in the position of Fermi level within the electronic structure cause the films to either exhibit unipolar n-type or p-type transport or move into a two-band regime where both electrons and holes contribute to conduction and the Seebeck coefficient becomes very small. Controlling host-guest interactions is therefore essential for optimising the thermoelectric properties. We also show evidence that the transport physics is governed by the structural heterogeneity of the films and that the conductivity is limited by grain boundary transport. However, the grain boundaries appear to have good interconnectivity and support efficient disordered metallic transport that enables reaching such high conductivities. With some further optimization of film quality and more advanced methods of Fermi level tuning 2D Ni-N based cCPs could become an attractive class of materials for thermoelectric as well as (bio)sensing applications. Coordination-cross-linked organic polymers could also be a potentially useful strategy for high-performing thermoelectric materials.[67]

6. Experimental Section

Materials: Nickel(II) acetylacetonate (Ni(acac)$_2$) was recrystallized prior to use. Ammonium hydroxide solution (28% NH$_3$ in H$_2$O) with 99.99% trace metals basis, was purchased from Sigma-Aldrich. 1,2,3,4,5,6-hexaaminobenzene trihydrochloride (HAB·3HCl) was purchased from Toronto Research Chemicals, and 2,3,6,7,10,11-hexaaminotriphenylene hexahydrochloride (HATP·6HCl) was purchased from BLDpharm. The synthesis of 2,3,7,8,12,13-hexaiminotriindole hexahydrochloride (HATI-H·6HCl) will be reported elsewhere,[68] while methyl 2,3,7,8,12,13-hexaiminotriindole hexahydrochloride (HATI-Me·6HCl) was synthesized following literature procedures.[12] Corning EAGLE XG glass substrates and front side-polished bare Si wafers (flat: SEMI Std.) were purchased from Corning Inc. and Active Business Company GmbH, respectively. Specially designed, commercially available silicon-based Linseis chips for thermal conductivity measurements were ordered from Linseis Messgeräte GmbH.

Synthesis: In a nitrogen-filled glovebox, Ni(acac)$_2$ was dissolved in degassed double-deionized water (DI water) at 60 °C, to prepare a solution with a concentration of 2.5 mmol L^{-1}, while 28% NH$_3$ in H$_2$O was diluted by 25 times and organic ligand was dissolved in DI water at a concentration of 1.8 mmol L^{-1} at room temperature. H$_2$O (6 mL), 25-time diluted NH$_3$ in H$_2$O (25–100 equiv., depending on the reactions), aqueous solution of Ni(acac)$_2$ (0.72–2.16 mL, i.e., 2–6 equiv., depending on the reactions), and aqueous solution of organic ligand (0.5 mL, 1 equiv.) were added into a small vial (volume 20 mL) in a sequence at ≈30 °C. After sealed with a non-air-tight cap, the reaction system was removed from the glovebox to ambient air and kept at 45 °C overnight (12 – 15 h), notably, minimising external, mechanical vibrations. Thin films formed on the surface were transferred onto O$_2$ plasma-treated substrates in air. The films were awaited to fully dry out before soaking them again in CHCl$_3$ for a couple of minutes. Finally, the films were checked under optical microscope. The whole process of transfer and observation, meaning exposure to air (under yellow light), was usually ≈1–1.5 h.

Scanning Electron Microscopy (SEM): The surface morphologies of the films were imaged using a Zeiss LEO 1550 field-emission SEM with a working distance of 3.5–4 mm, an acceleration voltage of 3 kV, and an in-lens detector. Samples were deposited on Si without thermal-growth oxide.

Raman Spectroscopy: Raman spectra were collected using a Horiba T64000 Raman spectrometer under a laser excitation of 633 nm in ambient air at room temperature. Samples were prepared on either 1 cm × 1 cm Si wafers without thermal-growth oxide or Corning EAGLE XG glass. Before acquisition, the spectrometer was calibrated with the characterized band

(520.70 cm^{-1}) of a standard Si sample. During acquisition, an integration time of no less than 30 s, 7 cycles, and a laser power that did not lead to visible beam damage were used.

Fourier Transform Infrared (FTIR) Spectroscopy: FTIR spectra were measured with a Bruker Vertex 70 V with a wide-band DLaTGS detector in transmission geometry under rough vacuum. 32 scans, 5 mm slit, and 2.5 kHz mirror scan rate (expressed in units of the sampling frequency of the interferogram) were employed during measurement. The samples were prepared on double-side-polished, highly resistive Si wafers.

X-Ray diffraction (XRD) and Grazing-Incidence Wide-Angle X-Ray Scattering (GIWAXS): Samples were prepared on 1 cm × 1 cm Si wafer without thermal-growth oxide. XRD was measured in a Bruker D8 Discover diffractometer in ambient air. Steps of 0.03 degree, integration time of 0.5 s, and power of 1600 W were used during measurements. GIWAXS measurements were performed at Diamond Light Source beamline I-07 at 12.5 keV X-ray beam energy. Images were collected using a Pilatus 2m camera positioned 450.5 mm from the sample. Sample-detector distance was calibrated using a silver behenate reference sample. All measurements were performed at an incidence angle of 0.2 degree, with samples mounted on a temperature-controlled stage inside a helium filled chamber with Kapton windows. Data was processed using the MATLAB package GIXSGUI.[69]

Device Fabrication: For room-temperature electrical conductivity and Seebeck coefficient measurements, a four-parallel-electrode device architecture was used. Substrates (Corning EAGLE XG, thickness ≈700 μm) were cleaned by sequential sonication steps in acetone, 2% Decon 90 / DI water, DI water, and isopropanol (10 minutes for each). Then washed substrates were dried with nitrogen gas and exposed to oxygen plasma at 300 W for 3–5 min. All electrical contacts, Cr/Au (4 nm/20 nm), were deposited on freshly prepared, cleaned substrates by thermal evaporation through shadow mask method. The synthetic films of coordination polymers were transferred onto them.

Room-Temperature Electrical Conductivity and Seebeck Coefficient Measurements: Measurements were performed on a manual probe station using an Agilent 4155B Semiconductor Parameter Analyzer for electrical conductivity measurement and using a Keithley Nanovoltmeter 2182A for Seebeck coefficient measurement under nitrogen atmosphere (Belle Technology, < 5 ppm O_2 and < 10 ppm H_2O). Each device was electrically isolated before measurement by carefully scratching off the film outside the active device area under an optical microscope. Film thickness was measured by surface profilometry.

Temperature-Dependent Thermoelectric Measurements: For temperature-dependent thermoelectric measurements (electrical conductivity, Seebeck coefficient, and thermal conductivity), the data was collected with a Linseis Thin-Film Analyzer. Films were deposited onto specially designed, commercially available silicon-based chips containing two free standing, different-area Si_3N_4 membranes (referred to as Linseis chips). In this device the electrical conductivity was measured using the four-point-probe Van der Pauw method. The Seebeck coefficient was measured by using an on-chip heater and thermometer which are two microfabricated electrical wires aligned with the longitudinal axes of the membranes. The heater and thermometer were also used in thermal conductivity measurements. For thermal conductivity measurements, a high width/thickness ratio of the membranes on which films covered ensures that the heat flux is predominantly horizontally and 1D across the sample and in line with the plane of the membranes. Thus, the measurements performed in this work probe the in-plane thermal conductivity of the samples by using a 3ω-based method.[70] By performing measurements on the two different-area membranes integrated on the same substrate, correction for radiative losses and subtraction of the contribution from empty membranes to total heat conduction (from membrane and sample) is allowed; accurate measurements are hence enabled. Calculation of these thermoelectric parameters was carried out on the raw data in the software of Linseis Thin-Film Analyzer according to the method developed by Linseis et al.[70]

DFT Calculation: DFT was performed using Gaussian 09 with the B3LYP functional and 6–311g(d,p) basis set and the Grimme D3 dispersion correction.[71] The conformations of the cCPs were optimized first, and then the H_2O or O_2 molecule was added into the system. As an ex-

ample, the information about how and where the H_2O or O_2 molecule was added is shown in Figure S20 (Supporting Information).

Supporting Information

Supporting Information is available from the Wiley Online Library or from the author.

Conflict of Interest

The authors declare no conflict of interest.

Data Availability Statement

The data that support the findings of this study are available from the corresponding author upon reasonable request.

[1] S. Batten, N. Champness, X.-M. Chen, J. Garcia-Martinez, S. Kitagawa, L. Öhrström, M. O'Keeffe, M. P. Suh, J. Reedijk, *Pure Appl. Chem.* **2013**, *85*, 1715.

[2] E. M. Miner, T. Fukushima, D. Sheberla, L. Sun, Y. Surendranath, M. Dincă, *Nat. Commun.* **2016**, *7*, 10942.

[3] R. G. Mariano, O. J. Wahab, J. A. Rabinowitz, J. Oppenheim, T. Chen, P. R. Unwin, M. Dincă, *ACS Cent. Sci.* **2022**, *8*, 975.

[4] M. Amores, K. Wada, K. Sakaushi, H. Nishihara, *J. Phys. Chem. C* **2020**, *124*, 9215.

[5] K. Wada, K. Sakaushi, S. Sasaki, H. Nishihara, *Angew. Chem., Int. Ed.* **2018**, *130*, 9024.

[6] D. Feng, T. Lei, M. R. Lukatskaya, J. Park, Z. Huang, M. Lee, L. Shaw, S. Chen, A. A. Yakovenko, A. Kulkarni, J. Xiao, K. Fredrickson, J. B. Tok, X. Zou, Y. Cui, Z. Bao, *Nat. Energy* **2018**, *3*, 30.

[7] S. Wang, Z. Xie, D. Zhu, S. Fu, Y. Wu, H. Yu, C. Lu, P. Zhou, M. Bonn, H. I. Wang, Q. Liao, H. Xu, X. Chen, C. Gu, *Nat. Commun.* **2023**, *14*, 6891.

**ADVANCED
SCIENCE NEWS**

www.advancedsciencenews.com

**ADVANCED
MATERIALS**

www.advmat.de

[8] Y. Su, B. Li, H. Xu, C. Lu, S. Wang, B. Chen, Z. Wang, W. Wang, K. I. Otake, S. Kitagawa, L. Huang, C. Gu, *J. Am. Chem. Soc.* **2022**, *144*, 18218.

[9] Y. He, C. D. Spataru, F. Léonard, R. E. Jones, M. E. Foster, M. D. Allendorf, A. A. Talin, *Phys. Chem. Chem. Phys.* **2017**, *19*, 19461.

[10] T. Deng, X. Yong, W. Shi, C. K. Gan, W. Li, K. Hippalgaonkar, J. C. Zheng, X. Wang, S. W. Yang, J. S. Wang, G. Wu, *Adv. Electron. Mater.* **2019**, *5*, 1800892.

[11] X. Yong, W. Shi, G. Wu, S. S. Goh, S. Bai, J. W. Xu, J. S. Wang, S. W. Yang, *J. Mater. Chem. A* **2018**, *6*, 19757.

[12] Y. Lu, Y. Zhang, C. Y. Yang, S. Revuelta, H. Qi, C. Huang, W. Jin, Z. Li, V. Vega-Mayoral, Y. Liu, X. Huang, D. Pohl, M. Položij, S. Zhou, E. Cánovas, T. Heine, S. Fabiano, X. Feng, R. Dong, *Nat. Commun.* **2022**, *13*, 7240.

[13] L. Sun, B. Liao, D. Sheberla, D. Kraemer, J. Zhou, E. A. Stach, D. Zakharov, V. Stavila, A. A. Talin, Y. Ge, M. D. Allendorf, G. Chen, F. Léonard, M. Dincă, *Joule* **2017**, *1*, 168.

[14] Z. Chen, Y. Cui, Y. Jin, L. Liu, J. Yan, Y. Sun, Y. Zou, Y. Sun, W. Xu, D. Zhu, *J. Mater. Chem. C* **2020**, *8*, 8199.

[15] Q. Zhao, S. H. Li, R. L. Chai, X. Ren, C. Zhang, *ACS Appl. Mater. Interfaces* **2020**, *12*, 7504.

[16] J. Zhang, G. Zhou, H.-I. Un, F. Zheng, K. Jastrzembski, M. Wang, Q. Guo, D. Mücke, H. Qi, Y. Lu, Z. Wang, Y. Liang, M. Löffler, U. Kaiser, T. Frauenheim, A. Mateo-Alonso, Z. Huang, H. Sirringhaus, X. Feng, R. Dong, *J. Am. Chem. Soc.* **2023**, *145*, 23630.

[17] J. Park, A. C. Hinckley, Z. Huang, D. Feng, A. A. Yakovenko, M. Lee, S. Chen, X. Zou, Z. Bao, *J. Am. Chem. Soc.* **2018**, *140*, 14533.

[18] Z. Wang, L. S. Walter, M. Wang, P. S. Petkov, B. Liang, H. Qi, N. N. Nguyen, M. Hambsch, H. Zhong, M. Wang, S. Park, L. Renn, K. Watanabe, T. Taniguchi, S. C. B. Mannsfeld, T. Heine, U. Kaiser, S. Zhou, R. T. Weitz, X. Feng, R. Dong, *J. Am. Chem. Soc.* **2021**, *143*, 13624.

[19] J. H. Dou, M. Q. Arguilla, Y. Luo, J. Li, W. Zhang, L. Sun, J. L. Mancuso, L. Yang, T. Chen, L. R. Parent, G. Skorupskii, N. J. Libretto, C. Sun, M. C. Yang, P. V. Dip, E. J. Brignole, J. T. Miller, J. Kong, C. H. Hendon, J. Sun, M. Dincă, *Nat. Mater.* **2021**, *20*, 222.

[20] D. G. Ha, M. Rezaee, Y. Han, S. A. Siddiqui, R. W. Day, L. S. Xie, B. J. Modtland, D. A. Muller, J. Kong, P. Kim, M. Dincă, M. A. Baldo, *ACS Cent. Sci.* **2021**, *7*, 104.

[21] R. W. Day, D. K. Bediako, M. Rezaee, L. R. Parent, G. Skorupskii, M. Q. Arguilla, C. H. Hendon, I. Stassen, N. C. Gianneschi, P. Kim, M. Dincă, *ACS Cent. Sci.* **2019**, *5*, 1959.

[22] X. Huang, P. Sheng, Z. Tu, F. Zhang, J. Wang, H. Geng, Y. Zou, C. A. Di, Y. Yi, Y. Sun, W. Xu, D. Zhu, *Nat. Commun.* **2015**, *6*, 7408.

[23] X. Huang, S. Zhang, L. Liu, L. Yu, G. Chen, W. Xu, D. Zhu, *Angew. Chem.* **2018**, *130*, 152.

[24] X. Chen, J. Dong, K. Chi, L. Wang, F. Xiao, S. Wang, Y. Zhao, Y. Liu, *Adv. Funct. Mater.* **2021**, *31*, 2102855.

[25] R. Toyoda, N. Fukui, D. H. L. Tjhe, E. Selezneva, H. Maeda, C. Bourgès, C. M. Tan, K. Takada, Y. Sun, I. Jacobs, K. Kamiya, H. Masunaga, T. Mori, S. Sasaki, H. Sirringhaus, H. Nishihara, *Adv. Mater.* **2022**, *34*, 2106204.

[26] J. H. Dou, L. Sun, Y. Ge, W. Li, C. H. Hendon, J. Li, S. Gul, J. Yano, E. A. Stach, M. Dincă, *J. Am. Chem. Soc.* **2017**, *139*, 13608.

[27] A. C. Hinckley, J. Park, J. Gomes, E. Carlson, Z. Bao, *J. Am. Chem. Soc.* **2020**, *142*, 11123.

[28] T. Chen, J. H. Dou, L. Yang, C. Sun, N. J. Libretto, G. Skorupskii, J. T. Miller, M. Dincă, *J. Am. Chem. Soc.* **2020**, *142*, 12367.

[29] K. Yuan, T. Song, X. Zhu, B. Li, B. Han, L. Zheng, J. Li, X. Zhang, W. Hu, *Small* **2019**, *15*, 1804845.

[30] Y. Zang, F. Pei, J. Huang, Z. Fu, G. Xu, X. Fang, *Adv. Energy Mater.* **2018**, *8*, 1802052.

[31] H. Jia, Y. Yao, J. Zhao, Y. Gao, Z. Luo, P. Du, *J. Mater. Chem. A* **2018**, *6*, 1188.

[32] D. Sheberla, L. Sun, M. A. Blood-Forsythe, S. Er, C. R. Wade, C. K. Brozek, A. Aspuru-Guzik, M. Dincă, *J. Am. Chem. Soc.* **2014**, *136*, 8859.

[33] K. H. Wu, J. Cao, T. Pal, H. Yang, H. Nishihara, *ACS Appl. Energy Mater.* **2021**, *4*, 5403.

[34] N. Lahiri, N. Lotfizadeh, R. Tsuchikawa, V. V. Deshpande, J. Louie, *J. Am. Chem. Soc.* **2017**, *139*, 19.

[35] G. Wu, J. Huang, Y. Zang, J. He, G. Xu, *J. Am. Chem. Soc.* **2017**, *139*, 1360.

[36] T. Kambe, R. Sakamoto, K. Hoshiko, K. Takada, M. Miyachi, J. H. Ryu, S. Sasaki, J. Kim, K. Nakazato, M. Takata, H. Nishihara, *J. Am. Chem. Soc.* **2013**, *135*, 2462.

[37] M. Wang, R. Dong, X. Feng, *Chem. Soc. Rev.* **2021**, *50*, 2764.

[38] S. Chen, J. Dai, X. C. Zeng, *Phys. Chem. Chem. Phys.* **2015**, *17*, 5954.

[39] T. Sick, J. M. Rotter, S. Reuter, S. Kandambeth, N. N. Bach, M. Döblinger, J. Merz, T. Clark, T. B. Marder, T. Bein, D. D. Medina, *J. Am. Chem. Soc.* **2019**, *141*, 12570.

[40] C. H. Feriante, S. Jhulki, A. M. Evans, R. R. Dasari, K. Slicker, W. R. Dichtel, S. R. Marder, *Adv. Mater.* **2020**, *32*, 1905776.

[41] R. A. Dodson, A. G. Wong-Foy, A. J. Matzger, *Chem. Mater.* **2018**, *30*, 6559.

[42] X. Sun, K. H. Wu, R. Sakamoto, T. Kusamoto, H. Maeda, X. Ni, W. Jiang, F. Liu, S. Sasaki, H. Masunaga, H. Nishihara, *Chem. Sci.* **2017**, *8*, 8078.

[43] X. Sun, K. H. Wu, R. Sakamoto, T. Kusamoto, H. Maeda, H. Nishihara, *Chem. Lett.* **2017**, *46*, 1072.

[44] M. R. Lukatskaya, D. Feng, S. M. Bak, J. W. F. To, X. Q. Yang, Y. Cui, J. I. Feldblyum, Z. Bao, *ACS Nano* **2020**, *14*, 15919.

[45] E. J. H. Phua, K. H. Wu, K. Wada, T. Kusamoto, H. Maeda, J. Cao, R. Sakamoto, H. Masunaga, S. Sasaki, J. W. Mei, W. Jiang, F. Liu, H. Nishihara, *Chem. Lett.* **2018**, *47*, 126.

[46] Y. Su, K. ichi Otake, J. J. Zheng, S. Horike, S. Kitagawa, C. Gu, *Nature* **2022**, *611*, 289.

[47] C. Gu, N. Hosono, J. J. Zheng, Y. Sato, S. Kusaka, S. Sakaki, S. Kitagawa, *Science* **2019**, *363*, 387.

[48] Y. Li, R. T. Yang, *Langmuir* **2007**, *23*, 12937.

[49] C. H. Ho, M. L. Valentine, Z. Chen, H. Xie, O. Farha, W. Xiong, F. Paesani, *Commun. Chem.* **2023**, *6*, 70.

[50] A. L. Sutton, L. Melag, M. M. Sadiq, M. R. Hill, *Angew. Chem., Int. Ed.* **2022**, *61*, e202208305.

[51] D. E. Jaramillo, A. Jaffe, B. E. R. Snyder, A. Smith, E. Taw, R. C. Rohde, M. N. Dods, W. DeSnoo, K. R. Meihaus, T. D. Harris, J. B. Neaton, J. R. Long, *Chem. Sci.* **2022**, *13*, 10216.

[52] M. De Lourdes Gonzalez-Juarez, C. Morales, J. I. Flege, E. Flores, M. Martin-Gonzalez, I. Nandhakumar, D. Bradshaw, *ACS Appl. Mater. Interfaces* **2022**, *14*, 12404.

[53] M. R. Momeni, Z. Zhang, D. Dell'Angelo, F. A. Shakib, *APL Mater.* **2021**, *9*, 051109.

[54] E. M. Miner, S. Gul, N. D. Ricke, E. Pastor, J. Yano, V. K. Yachandra, T. Van Voorhis, M. Dincă, *ACS Catal.* **2017**, *7*, 7726.

[55] J. Park, Z. Chen, R. A. Flores, G. Wallnerström, A. Kulkarni, J. K. Nørskov, T. F. Jaramillo, Z. Bao, *ACS Appl. Mater. Interfaces* **2020**, *12*, 39074.

[56] K. N. Le, C. H. Hendon, *Phys. Chem. Chem. Phys.* **2019**, *21*, 25773.

[57] P. Apostol, S. M. Gali, A. Su, D. Tie, Y. Zhang, S. Pal, X. Lin, V. R. Bakuru, D. Rambabu, D. Beljonne, M. Dinca, A. Vlad, *J. Am. Chem. Soc.* **2023**, *145*, 24669.

[58] S. Dongmin Kang, G. Jeffrey Snyder, *Nat. Mater.* **2017**, *16*, 252.

[59] S. A. Gregory, R. Hanus, A. Atassi, J. M. Rinehart, J. P. Wooding, A. K. Menon, M. D. Losego, G. J. Snyder, S. K. Yee, *Nat. Mater.* **2021**, *20*, 1414.

[60] B. K. Chang, J. J. Zhou, N. E. Lee, M. Bernardi, *npj Comput. Mater.* **2022**, *8*, 63.

[61] N. Van Lien, D. Dinh Toi, *Phys. Lett. A* **1999**, *261*, 108.

[62] M. Cutler, N. F. Mott, *Phys. Rev.* **1969**, *181*, 1336.

**ADVANCED
SCIENCE NEWS**

www.advancedsciencenews.com

**ADVANCED
MATERIALS**

www.advmat.de

[63] N. F. Mott, E. A. Davis, *Electronic Processes in Non-Crystalline Materials*, Oxford University Press, Oxford **2012**.

[64] A. G. Zabrodskii, K. N. Zinov'eva, *Sov. Phys. JETP* **1984**, *59*, 425.

[65] A. B. Kaiser, *Adv. Mater.* **2001**, *13*, 927.

[66] A. B. Kaiser, *Phys. Rev. B* **1989**, *40*, 2806.

[67] C. Liu, X. Yin, S. Wang, C. Gao, L. Wang, *Chem. Eng. J.* **2023**, *451*, 138751.

[68] Y. Lu, Z. Hu, P. Petkov, S. Fu, H. Qi, C. Huang, Y. Liu, X. Huang, M. Wang, P. Zhang, U. Kaiser, M. Bonn, H. I. Wang, P. Samori, E. Coronado, R. Dong, X. Feng, *J. Am. Chem. Soc.* **2024**, https://doi.org/10.1021/jacs.3c11172.

[69] Z. Jiang, *J. Appl. Cryst.*. **2015**, *48*, 917.

[70] V. Linseis, F. V¨olklein, H. Reith, K. Nielsch, P. Woias, *Rev. Sci. Instrum.* **2018**, *89*, 015110.

[71] Gaussian 09, Revision C.01, M. J. Frisch, G. W. Trucks, H. B. Schlegel, G. E. Scuseria, M. A. Robb, J. R. Cheeseman, G. Scalmani, V. Barone, B. Mennucci, G. A. Petersson, H. Nakatsuji, M. Caricato, X. Li, H. P. Hratchian, A. F. Izmaylov, J. Bloino, G. Zheng, J. L. Sonnenberg, M. Hada, M. Ehara, K. Toyota, R. Fukuda, J. Hasegawa, M. Ishida, T. Nakajima, Y. Honda, O. Kitao, H. Nakai, T. Vreven, J. A. Montgomery Jr., et. al., Gaussian, Inc., Wallingford CT, **2010**.